COMPUTATIONAL PHANTOM FOR THE DOSIMETRY OF THE RED BONE MARROW OF A 10-YEAR-OLD CHILD DUE TO INCORPORATED BETA-EMITTERS

Sharagin PA[1] ✉, Tolstykh EI[1], Shishkina EA[1,2]

[1] Urals Research Center for Radiation Medicine of the Federal Medical-Biological Agency, Chelyabinsk, Russia

[2] Chelyabinsk State University, Chelyabinsk, Russia

Bone-seeking radionuclides, in particular ^{89,90}Sr, could get into the environment in the course of various anthropogenic radiation incidents. From there they enter a human body with food and water. This leads to red bone marrow (RBM) internal exposure. These elements were present in the composition of radioactive releases into the Techa River in 1950s, and are the major source of RBM exposure for the residents of the riverside settlements. RBM dose estimation relies on dosimetric modeling which comprises the development of 3D computational phantoms of the skeleton parts. By imitating the energy transfer in these phantoms, the conversion coefficients from the radionuclide activity in a bone to the dose rate in RBM are evaluated. The given study is yet another step in the research aimed at the elaboration of a set of computational phantoms of the skeleton for people of various age. The objective is to develop a computational phantom of a skeleton of a 10-year-old child to estimate dose to RBM due to incorporated beta-emitters. Original SPSD (stochastic parametric skeletal dosimetry) approach was used to create the phantoms. According to this method the skeleton sites containing RBM were divided into smaller segment of simple geometric shape, for which voxel phantoms were generated. The parameters for phantom generation were based on published research data. They included linear dimensions of bones, thickness of the cortical layer, characteristics/properties of the bone micro-architecture, density and chemical composition of the modelled media and the percentage of RBM content in bones. Generated computational phantom of the skeleton sites with active hematopoiesis of a 10-year-old child consists of 38 phantom-segments. Linear dimensions of the segments were from 3 to 88 mm, cortical layer thickness: 0.2–2.2 mm.

Keywords: trabecular bone, cortical bone, bone marrow dosimetry, computational phantoms, Sr

Funding: the study was performed within the framework of the Federal Target Program "Ensuring Nuclear and Radiation Safety for 2016–2020 and the Period up to 2035" and supported by the Federal Medical Biological Agency of Russia.

Author contribution: Sharagin PA — data acquisition, analysis, and interpretation; manuscript drafting and revising. Tolstykh EI — study methodology elaboration, manuscript revising and approval; Shishkina EA — study design and concept development, manuscript revising and approval.

✉ **Correspondence should be addressed:** Pavel A. Sharagin
Vorovskogo, 68-a, Chelyabinsk, 454141, Russia; sharagin@urcrm.ru

Received: 20.05.2024 **Accepted:** 21.06.2024 **Published online:** 29.06.2024

DOI: 10.47183/mes.2024.032

ВЫЧИСЛИТЕЛЬНЫЙ ФАНТОМ ДЛЯ ДОЗИМЕТРИИ КРАСНОГО КОСТНОГО МОЗГА ДЕСЯТИЛЕТНЕГО РЕБЕНКА ОТ ИНКОРПОРИРОВАННЫХ БЕТА-ИЗЛУЧАТЕЛЕЙ

П. А. Шарагин[1] ✉, Е. И. Толстых[1], Е. А. Шишкина[1,2]

[1] Уральский научно-практический центр радиационной медицины Федерального медико-биологического агентства России, Челябинск, Россия

[2] Челябинский государственный университет, Челябинск, Россия

Остеотропные радионуклиды, в частности ^{89,90}Sr, могут попадать в окружающую среду при различных техногенных радиационных инцидентах, оттуда с пищей и водой они поступают в организм человека, что приводит к внутреннему облучению красного костного мозга (ККМ). Эти элементы были в составе радиоактивных сбросов в реку Теча в 1950-е гг., и являются основным источником облучения ККМ жителей прибрежных территорий. Оценка доз на ККМ опирается на дозиметрическое моделирование, которое включает разработку трехмерных вычислительных фантомов частей скелета. На основе имитации переноса энергии в этих фантомах оценивают коэффициенты перехода от активности радионуклида в кости к мощности дозы в ККМ. Целью исследования было разработать вычислительный фантом скелета десятилетнего ребенка для оценки доз на ККМ от инкорпорированных бета-излучателей. Для создания фантомов использовали оригинальный SPSD (от англ. stochastic parametric skeletal dosimetry) подход. Согласно данной методике, участки скелета, содержащие ККМ, разбивались на меньшие сегменты простой геометрической формы, для которых генерировались воксельные фантомы. Параметры для генерации фантомов основаны на опубликованных данных, они включали: линейные размеры костей, толщину кортикального слоя, характеристики костной микроархитектуры, плотность и химический состав моделируемых сред и долю содержания ККМ в костях. Сгенерированный вычислительный фантом участков скелета с активным гемопоэзом десятилетнего ребенка состоит из 38 фантомов-сегментов. Линейные размеры сегментов были 3–88 мм, толщина кортикального слоя — 0,2–2,2 мм.

Ключевые слова: трабекулярная кость, кортикальная кость, дозиметрия костного мозга, вычислительные фантомы, Sr

Финансирование: работа выполнена в рамках реализации Федеральной целевой программы «Федеральная целевая программа «Обеспечение ядерной и радиационной безопасности на 2016–2020 годы и на период до 2035 года» и при финансовой поддержке Федерального медико-биологического агентства России.

Вклад авторов: П. А. Шарагин — получение, анализ и интерпретация данных, написание статьи; Е. И. Толстых — разработка методики исследования, редактирование статьи; Е. А. Шишкина — разработка концепции, редактирование статьи.

✉ **Для корреспонденции:** Павел Алексеевич Шарагин
ул. Воровского, д. 68-а, г. Челябинск, 454141, Россия; sharagin@urcrm.ru

Статья получена: 20.05.2024 **Статья принята к печати:** 21.06.2024 **Опубликована онлайн:** 29.06.2024

DOI: 10.47183/mes.2024.032

Internal exposure of the red bone marrow (RBM) due to bone-seeking radionuclides may lead to serious health effects for a human body. The most dangerous and wide-spread bone-seeking radionuclides are ^{89,90}Sr. These elements could be found in the composition of the global radioactive fallouts as a result of the nuclear weapon testing. They also got into the environment due to some other radiation incidents [1]. For example, strontium isotopes were present in the composition

of the radioactive releases into the Techa River in 1950s leading to their accumulation in the bodies of the residents of territories along the river [2–5]. It was ^{89,90}Sr that were the main sources of the RBM exposure for the members of the Techa River Cohort. Estimation of doses from these radionuclides is a challenging task. It involves biokinetic modeling of the radionuclide turnover to evaluate its concentration in a bone (source-tissue) [6], as well as dosimetric modeling which allows assessing the dose conversion factors (DF) from the radionuclide activity in a bone to the absorbed dose rate in RBM. Dosimetric models imitate the location of the source-tissue and target-tissue relative each other. At present computational phantoms (3D models of the skeleton and RBM) serve the function of such models. The radiation transfer is imitated inside these phantoms. Modern skeletal phantoms to estimate RBM doses are based on the analysis of the computer tomography (CT) images of the skeletons of very few deceased people [7–13].

Limited amount of biopsy material does not allow assessing the uncertainties associated with the variability of the size and micro-architecture of the skeleton within the population. As an alternative URCRM has developed an original parametric method of stochastic modeling of bone structures — SPSD-modeling (Stochastic parametric skeletal dosimetry) [14, 15]. Within the framework of this approach, it is suggested that numerous published measurement results of morphometric and hystomorphometric studies of the bones should be used as model parameters. High degree of statistical significance of the published measurement results makes it possible to estimate uncertainties associated with the individual variability of the skeletal parameters.

SPSD-phantom of a skeleton as a whole is a set of small phantom segments. These are the digital models of simple geometric shape filled with trabecular bone with RBM located in the inter-trabecular cavities. Some part of the phantom surfaces is covered with the layer of solid cortical bone. Thus, SPSD-phantoms contain two source-tissues: trabecular and cortical bone and one target-tissue — RBM. This model suits perfectly the internal dosimetry of bone-seeking beta-emitters [14, 15]. Model adequacy is supported by good agreement of the calculated energy dependences for the SPSD-phantoms and similar dependences described in some published research [14, 16, 17].

In case of population exposure, the radionuclides may enter a body of a person of various age. For example, radioactive contamination of the Techa River led to the exposure of residents in the age-range from newborns to elderly people [2–4, 18]. To estimate doses to RBM for all age groups we have previously developed SPSD-phantoms representing the skeleton of a new-born [19], one-year-old [20], and five-year-old child [21]. The objective of the current study is to develop computational phantoms representing the skeleton of a ten-year-old child to estimate RBM doses from beta-emitting radionuclides incorporated in a bone. The study is yet another step in the work aimed at the development of a set of computational phantoms of a standard man for different age groups.

METHODS

Computational phantom of a ten-year-old child was generated within the framework of SPSD method similarly to the phantoms for younger age groups [14]. The method consists of the following steps:

1) evaluation of the RBM distribution within the skeleton, identification of the modeled sites of the skeleton with active hematopoiesis (hematopoietic sites);

2) measuring linear dimensions and micro-structure parameters of the modeled bones based on the published data;

3) hematopoietic site segmentation;

4) voxel phantom generation for every segment.

Bone marrow distribution within the skeleton of 10-years-old child was evaluated using ICRP-data [13], which based on results of MRI-research [22].

In total the analysis included 11,927 measurement results of the bone samples [23, 24]. To measure the morphometric parameters of the phantoms of a ten-year-old child, manuscripts published in peer-reviewed journals, atlases, manuals, monographs, and dissertations were studied as well as digital resources containing collections of x-ray images. The measurement results of individuals/samples that the authors considered to be healthy and having no disorders resulting in bone deformities were used for the analysis. Ethnicity: Caucasians and Mongoloids, since these groups are typical of the Urals region. The subjects' age was 8–12 years.

Histomorphometry and micro-CT data were used to estimate the parameters of trabecular bone (*Tb. Th.*, *Tb. Sp.*, *BV/TV*) and cortical layer thickness. The following properties of the bone micro-architecture were evaluated: trabecular thickness (*Tb. Th.*), trabecular separation (*Tb. Sp.*), bone volume to total spongiosa volume relation (*BV/TV*). The data of the linear dimension measurement results of the skeletal bones were examined with the help of various techniques: micrometers, osteometric boards, ultrasound scans and radiography, as well as computed tomography (CT).

Within each skeletal site with active hematopoiesis the bones are subdivided into relatively small segments. The so-called Bone Phantom Segments (BPS) was modeled for every segment [25, 26]. Each segment should have relatively homogeneous microarchitecture and cortical layer thickness. Segments should be described by simple geometric shapes (cylinder, rectangular parallelepiped, etc.). Such subdivision allows taking into account the micro-architecture heterogeneity inside a bone. Moreover, relatively small size of the segments makes it possible to generate the phantoms imitating them with rather high resolution.

Averaged estimates of bone characteristics were taken as computational phantom parameters. If the published data on individual measurements were available, they were combined to calculate the means and standard deviations (SD). When the measurement results of groups of people were averaged, a weighting factor (W_N) which took account of the number of subjects (N) was introduced for each group: $W_N = 1$, when $N \geq 25$; $W_N = N/25$, when $N < 25$. Methods to select and assess the published data were previously described in detail in [23].

Linear dimensions and parameters of the bone micro-architecture influence the geometry of source and target tissue in BPS. They were determined for each segment separately. In addition to these parameters, the chemical composition and density of the modeled media were determined based on the published research data [27, 28] and were used for all the BPS of a ten-year-old child.

A voxel BPS was generated for each segment using the original Trabecula software [29]. Every voxel in a BPS imitates either mineralized bone, or bone marrow (BM), depending on the voxel center position in a phantom.

Trabecular (TB) and cortical bone (CB) were considered as source tissues, while bone marrow (BM) was viewed as target tissue. BM was uniformly distributed across the trabeculae in the BPS. Voxel size was selected individually for each phantom. It did not exceed 70% of trabecular thickness and varied in the

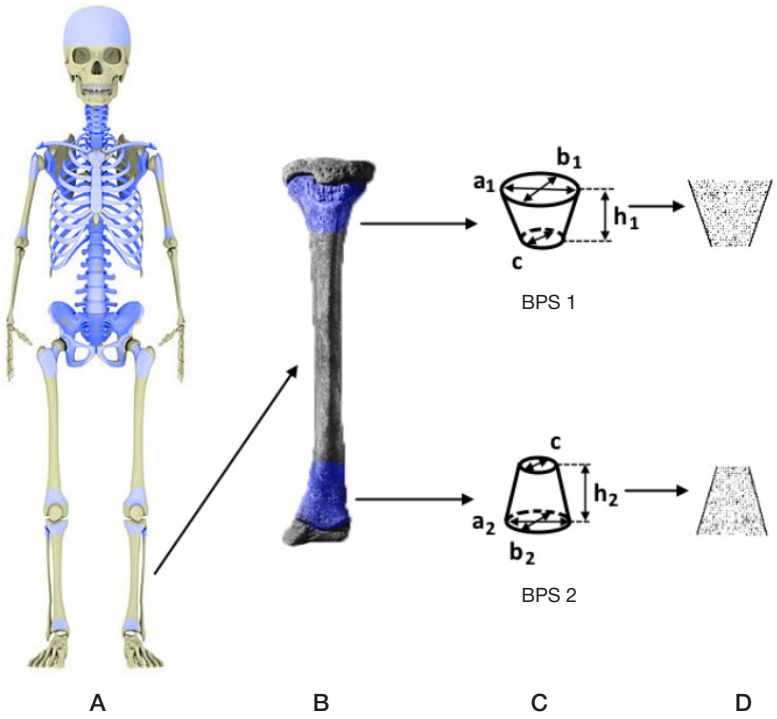

Fig. 1. Segmentation of the skeletal hematopoietic sites of a ten-year-old child using the example of the tibia. **A**. Skeleton of a ten-year-old child (modeled skeletal sites with active hematopoiesis are highlighted in *blue*). **B**. Tibia (modeled skeletal sites with active hematopoiesis are highlighted in *blue*). **C**. Scheme of bone division into BPS and BPS linear dimensions. **D**. BPS of the tibia — voxel representation, cross section (voxels simulating bone tissue are highlighted in *black*, those simulating RBM are highlighted in *white*)

range 50–200 μm [29, 30]. The modeled media volumes were calculated for each BPS using the Trabecula software package.

Hematopoietic sites of a ten-year-old child, segmentation process and generated BPS are given in Fig. 1 (exemplified by the tibia).

SPSD method allows simulating the population variability of the micro-structure sizesand characteristics for every BPS. With this objective in view, 12 Supplementary Phantom Segments (SPS) were created for every BPS with the bone micro- and macro-structure parameters randomly selected within the range of their individual variability (within the limits of minimum and maximum measured values).

RESULTS

Skeletal sites with active hematopoiesis of the skeleton of a ten-year-old child and RBM mass fraction in these sites have been determined based on the ICRP data [22] and are provided in Table 1.

As it can be seen from Table 1, the skeleton of a ten-year-old child has 13 hematopoietic sites. RBM mass fraction in these sites varies from 0.9% to 18.1% of the total RBM content in the skeleton. In addition, distribution of RBM within each hematopoietic site was determined based on the published MRI data [31–36].

Chemical composition of the modeled media was obtained based on the ICRP data for adults (Table 2) [25].

The density of mineral bone tissue has been estimated based on the measurement results of the cortical bone thickness in children aged 10 and is equal to 1.85 g/cm^3 [26]. It has been assumed that RBM density is equal to that of water (1 g/cm^3) [25].

Bone micro-structure characteristics were evaluated based on the published research data. A detailed description of their

Table 1. Mass fraction of RBM (% of the total mass of RBM in the skeleton) in the main hematopoietic sites of a ten-year-old child's skeleton [13, 22]

№	Hematopoietic site	RBM mass fraction, %
1	Femur	15.7
2	Humerus	4.1
3	Sacrum	6.8
4	Tibia bones	5.6
5	Pelvic bones	15.8
6	Skull	12.8
7	Clavicle	0.9
8	Scapula	2.9
9	Sternum	1.8
10	Ribs	11
11	Cervical vertebrae	2.7
12	Thoracic vertebrae	11
13	Lumbar vertebrae	8.5

Table 2. Chemical composition of simulated media adopted for all BPS

Chemical composition, rel. units		
Chemical element	Bone	Active marrow
H	0.035	0.105
C	0.16	0.414
N	0.042	0.034
O	0.445	0.439
Na	0.003	0.001
Mg	0.002	0.002
P	0.095	0.002
S	0.003	0.002
Ca	0.215	–

analysis and calculation of the population-average were given in [23]. Micro-architecture parameter values for the BPS of a ten-year-old child are provided in Table 3.

Linear dimensions and values of cortical layer thickness assumed for the BPS of a ten-year-old child are given in Table 4.

As it is shown in Table 4 the phantom of hematopoietic sites of a ten-year-old child skeleton consists of 38 BPS. The number of BPS within a hematopoietic site depended on its shape and varied from 1 (ribs) to 9 (pelvic bones).

Most of the BPSs of a ten-year-old child were represented by cylinders and rectangular parallelepipeds. Their linear dimensions were within the range from 3 to 88 mm. The minimum *Ct. Th*. value was reported for the BPSs of the vertebra (0.2 mm). It differed tenfold from the maximum value assumed for the proximal end of the femora (2.2 mm). Bone micro-architecture parameters also varied widely. *BV/TV* value in BPS varies in the range 14-52%, *Tb. Th* — from 0.12 mm to 0.29 mm, *Tb. Sp.* — from 0.46 mm to 1 mm (Table 3).

On the average, individual variability of the BPS linear dimensions made up 12%. The greatest variability was reported for the iliac bone (30%), the least — for the lateral border of scapula. The cortical layer thickness of the bone varied within the range from 7% (cervical vertebra) to 62% (sternum). On the average, it made up 24%. The variability of the micro-structure parameters was within the range 6–42%, and on the average it was 19%. The obtained values of the variability parameters of the phantoms were used to model SPS. The volume of the SPS could differ from the volume of the BPS more than 3 times both upwards or downwards. Calculation of the DF for the BPSs and SPSs will make it possible to evaluate DF population variability as a mean-square deviation of the DF values calculated for SPS from those calculated for the BPS.

DISCUSSION

The phantom of a skeleton of a ten-year-old child has less BPSs than that of a five-year-old child. It could be explained by the fact that RBM has been substituted by yellow bone marrow in the tubular bone diaphyses, therefore these skeletal sites were not modeled. At the age of 10 the greatest RBM fraction is located in the pelvic bones and femora as compared to the younger age groups when the greatest amount of RBM is reported for the cranial bones. Also, at this age 29% of the total RBM is reported for the segments of the spine and sacrum. Micro-structure parameters of the BPS change little as compared to the phantom of a five-year-old child. There is a tendency to a decrease in *BV/TV* and *Tb.Th*, and an increase in *Tb. Sp*. Over a 5-year period, i.e. by the age of 10, the cortical layer thickness has increased by 20% in any given BPS. The age-dependent changes in the characteristics of the phantoms could be demonstrated by comparing the volumes of the simulated media. Table 5 shows the comparison of the volume of the skeletal sites of five- and ten-year old child on the example of the distal end of the femur, clavicle, cervical and lumbar vertebra.

Table 3. Micro-architecture parameters assumed for BPS of a ten-year-old-child [11, 34–56] (coefficient of variation (CV) is given in parentheses, %)

Hematopoietic site	*BV/TV*, %	*Tb. Th*, mm	*Tb. Sp*, mm
Femur (proximal part)	35 (22–53)	0.24 (22)	0.54 (14)
Femur (distal part)	26 (17–40)		
Humerus	22 (13–37)	0.21 (13)	0.58 (32)
Ribs	20 (10–37)	0.23 (34)	0.5 (14)
Tibia bones*	25 (20–31)	0.21 (13)	0.74 (11)
Pelvic bones (ilium)	25 (20–31)	0.16 (10)	0.46 (15)
Other pelvic bones	25 (20–31)	0.16 (10)	0.6 (12)
Skull*	52 (41–65)	0.29 (32)	0.57 (35)
Clavicle (central part)	15 (10–23)	0.2 (32)	0.8 (25)
Clavicle (end's)	29 (15–46)	0.15 (13)	0.8 (25)
Scapula*	22 (6–38)	0.24 (42)	0.96 (23)
Sternum*	15 (7–23)	0.15 (27)	1.0 (6)
Cervical vertebrae	21 (12–35)	0.14 (14)	0.65 (24)
Thoracic vertebrae + lumbar vertebrae + sacrum	14 (7–26)	0.12 (17)	0.65 (24)

Note: * — micro-architecture parameters were calculated based on the measurement results of similar bones or based on the data for other age groups; the calculation method was reported previously in [23].

Table 4. Linear dimensions and cortical layer thickness assumed for the BPS representing a ten-year-old child

Hematopoietic site	Segment	Shape[1]	Phantom parameters, mm (CV is given in parentheses, %)[2]						Data sources
			h	*a*	*b*	*c*	*d*	*Ct.Th.*	
Бедро	Proximal end (upper part)	c	30	25 (7)	25 (7)			1.8 (17)	[56–64]
	Proximal end (lower part)	c	30	25 (7)	25 (7)			2.2 (12)	
	Distal end	dc	69 (5)	78 (7)	33 (10)	21 (9)	21 (9)	1.1 (14)	
Humerus	Proximal end	dc	27 (4)	39 (4)	33 (5)	18 (4)	18 (4)	1.1 (16)	[57–61, 65]
	Distal end	dc	27 (4)	54 (9)	18 (4)	18 (4)	18 (4)	0.8 (10)	
Ribs	Ribs[4]	p	10 (16)	30	5 (10)			0.7 (20)	[66, 67]
Sacrum	Body of the 1st vertebra	p	22 (20)	88 (20)	26 (10)			0.9 (34)	[68–73]
	Body of the 2nd vertebra	p	20 (20)	70 (20)	15 (10)			0.9 (34)	
	Body of the 3rd vertebra	p	18 (20)	62 (20)	10 (10)			0.9 (34)	
	Body of the 4th vertebra	p	13 (20)	53 (20)	7.7 (10)			0.9 (34)	
	Body of the 5th vertebra	p	13 (20)	44 (20)	7.7 (10)			0.9 (34)	
Tibia bones	Fibula proximal end[4]	c	30	11 (6)	11 (6)			1.7 (12)	[58, 70, 72]
	Tibia proximal end	dc	49 (6)	63 (7)	32 (20)	21 (6)	21 (6)	0.7 (11)	[57, 58, 74–77]
	Tibia distal end	dc	48 (6)	35 (12)	35 (12)	21 (6)	21 (6)	0.7 (11)	
Pelvic bones	Ilium part 1	p	8 (22)	30	30			1.7 (33) 0.9 (19)[3]	[78–85]
	Ilium part 2	p	8 (22)	30	30			0.9 (19)	
	Acetabular part of the ilium	dc	26 (7)	44 (7)	20 (22)	37 (3)	28 (30)	0.9 (17)	
	Acetabular part of the pubis	dc	9.8 (15)	28 (9)	21 (10)	16 (9)	11 (10)	0.5 (30)	
	Pubis bone (superior ramus)	c	39 (15)	16 (9)	11 (10)			0.5 (30)	
	Pubis bone (inferior ramus)	c	32 (15)	11 (10)	11 (10)			0.5 (30)	
	Acetabular part of the ischium	pr	29 (15)	28 (7)	29 (15)	28 (7)		0.5 (30)	
	Ischial tuberosity	c	34 (15)	19 (15)	19 (15)			0.5 (30)	
	Inferior ramus of the ischium	c	32 (15)	11 (10)	11 (10)			0.5 (30)	
Skull	Flat bones[4]	p	4.6 (18)	30	30			1.2 (18)	[86, 87]
Clavicle	Body[4]	c	30	11 (12)	8.3 (10)			1.8 (26)	[88–90]
	Sternal end	dc	17 (7)	22 (11)	20 (11)	11 (12)	8.3 (10)	0.8 (26)	
	Acromial end	dc	17 (7)	19 (11)	11 (23)	11 (12)	8.3 (10)	0.8 (26)	
Scapula	Glenoid	c	15 (5)	28 (5)	20 (7)			0.9 (28)	[91–93]
	Acromion	p	8.2 (18)	27 (8)	21 (8)			0.8 (13)	
	Lateral border	p	30	3.5 (3)	10 (12)			0.8 (13)	
Sternum	Sternum	p	8.5 (15)	30	30			0.7 (62)	[39, 94, 95]
Cervical vertebrae	Vertebral body	c	9.4 (12)	14 (7)	19 (13)			0.2 (7)	[79, 96, 97]
Thoracic vertebrae	Vertebral body	c	14 (17)	22 (21)	27 (24)			0.2 (25)	[98–101]
	Transverse process	p	8.6 (21)	13 (21)	7.3 (21)			0.2 (25)	
	Spinous process	p	7.2 (21)	25 (21)	4.1 (21)			0.2 (25)	
Lumbar vertebrae	Vertebral body	c	19 (18)	27 (21)	36 (21)			0.2 (25)	[73, 98, 99, 102]
	Transverse process	p	8.6 (20)	16 (20)	5.2 (20)			0.2 (25)	
	Spinous process	p	17 (20)	27 (20)	5.2 (20)			0.2 (25)	

Note: [1] — phantom shape was designated as follows: c — cylinder, dc — deformed cylinder, p — rectangular parallelepiped, [2] pr – prism with triangle base — BPS dimensions were designated as follows: *h* — height; *a* — major axis (c), major axis for a larger base (dc) or side a (p); *b* — minor axis (c), minor axis for a large base (dc) or side b (p); *c* — major axis for a small base (dc); *d* — minor axis for a small base (dc); for prism (pr): *a*, *b*, *c* — the sides of the prism base; [3] — cortical layer thickness was considered to be different for the inner (medial) and outer (gluteal) surfaces of this segment of the ilium; [4] — BPS imitated only a part of the simulated bone segment, when the bone segment dimensions significantly exceeded 30 mm, since in such cases it makes no sense to simulate the entire bone fragment in terms of dosimetry [15, 24].

It has been shown in Table 5 that the volume of the modeled media of a ten-year-old child exceeds that for a five-year-old one, which reflects the growth of the skeletal bones. The source-tissue volume increased on the average 1.96 times for TB, and 1.48 times for the CB. The total volume of the BPS increased 1.6 times over a 5-year period (from the age of 5 till 10). Over the same period of time the total volume of the CB increased only 1.3 times. It is due to the cessation of the hematopoiesis in skeletal sites with high *Ct.Th*. (the middle of the diaphyses of the long tubular bones). We expect that such age-dependent dynamics of the phantom characteristics will result in the decrease of the DF from Sr incorporated in the cortical bone.

In the course of the future studies the phantom parameters (Table 3, 4) provided in this manuscript will be integrated into the Trabecula software package to generate voxel phantom. The simulation of the energy transfer in these phantoms will allow estimating he DF for the bone-seeking beta-emitters, which gives an opportunity to estimate the RBM absorbed dose rate.

Table 5. Comparison of BPS volumes of five- and ten-year-old children

BPS	Simulated medium	Modeled structure volume, cm^3		
		5 years	10 years	10/5 years
Distal end of the femur	BM	22.9	49.94	2.18
	TB	7.56	17.49	2.31
	CB	5.21	8.97	1.72
	Entire BPS	35.67	76.4	2.14
Sternal end of the clavicle	BM	0.89	1.8	2.02
	TB	0.36	0.73	2.03
	CB	0.22	0.58	2.64
	Entire BPS	1.47	2.53	1.72
Body of the lumbar vertebra	BM	8.51	12.42	1.46
	TB	1.34	1.97	1.47
	CB	0.3	0.38	1.27
	Entire BPS	10.15	14.77	1.46
Body of the cervical vertebra	BM	0.89	1.43	1.61
	TB	0.24	0.38	1.58
	CB	0.05	0.07	1.4
	Entire BPS	1.18	1.88	1.59

CONCLUSIONS

As a result of the conducted study computational phantoms of the main skeletal sites with active hematopoiesis have been developed for a ten-year-old child. These phantoms were elaborated based on the SPSD method similar to the phantoms developed for other age groups. The obtained phantoms imitate the structure of the bone tissue. These sets demonstrate the population variability of the dimensions of the structure of certain skeletal bones. The provided phantom representing a ten-year-old child will further be used to calculate DF for ^{89,90}Sr, which in their turn are necessary for the assessment of the improved coefficients linking the individual radionuclide intake to dose to RBM. It will enable the dose estimates improvement for the residents of the Urals region. For the future studies we plan to develop SPSD-phantoms of the skeleton of men and women aged 15, and for adults. The given phantoms could be used for the dosimetry of incorporated bone-seeking beta-emitters in the population, in case of the contamination of the environment with radionuclides, and for the dosimetry of other beta-emitting radionuclides including those used in radionuclide therapy, such as ^{89}Sr, ^{32}P, ^{186}Re, ^{188}Re, ^{117}mSn.

References

1. Sources and effects of ionizing radiation. UNSCEAR 2000 Report to the General Assembly, with Scientific Annexes/ United Nations. New York, 2000; 1229 c.
2. Degteva MO, Shagina NB, Vorobiova MI, Shishkina EA, Tolstykh EI, Akleyev AV. Contemporary Understanding of Radioactive Contamination of the Techa River in 1949–1956. Radiats Biol Radioecol. 2016; 56 (5): 523–34. PMID: 30703313.
3. Krestinina LY, Epifanova S, Silkin S, Mikryukova L, Degteva M, Shagina N, et al. Chronic low-dose exposure in the Techa River Cohort: risk of mortality from circulatory diseases. Radiat Environ Biophys. 2013; 52 (1): 47–57. DOI: 10.1007/s00411-012-0438-5. Epub 2012 Nov 4.
4. Akleev AV. Hronicheskij luchevoj sindrom u zhitelej pribrezhnyh sel reki Techa. Cheljabinsk: Kniga, 2012; 464 s. Russian.
5. Preston DL, Sokolnikov ME, Krestinina LY, Stram DO. Estimates of Radiation Effects on Cancer Risks in the Mayak Worker, Techa River and Atomic Bomb Survivor Studies. Radiat Prot Dosimetry. 2017; 173 (1–3): 26–31. DOI: 10.1093/rpd/ncw316.
6. Degteva MO, Napier BA, Tolstykh EI, et al. Enhancements in the Techa River Dosimetry System: TRDS-2016D Code for Reconstruction of Deterministic Estimates of Dose From Environmental Exposures. Health Phys. 2019; 117 (4): 378–87. DOI: 10.1097/HP.0000000000001067.
7. Spiers FW, Beddoe AH, Whitwell JR. Mean skeletal dose factors for beta-particle emitters in human bone. Part I: volume-seeking radionuclides. The British journal of radiology. 1978; 51 (608): 622–7.
8. O'Reilly SE, DeWeese LS, Maynard MR, Rajon DA, Wayson MB, Marshall EL, et al. An 13 image-based skeletal dosimetry model for the ICRP reference adult female-internal electron 14 sources. Phys Med Biol. 2016; 61 (24): 8794–24. Epub 2016 Nov 29.
9. Xu XG, Chao TC, Bozkurt A. VIP-Man: an image-based whole-body adult male model constructed from color photographs of the Visible Human Project for multi-particle Monte Carlo calculations. Health Phys. 2000; 78 (5): 476–86. DOI: 10.1097/00004032-200005000-00003. PMID: 10772019.
10. Shah AP, Bolch WE, Rajon DA, Patton PW, Jokisch DW. A paired-image radiation transport model for skeletal dosimetry. J Nucl Med. 2005; 46 (2): 344–53. PMID: 15695796.
11. Pafundi D. Image-based skeletal tissues and electron dosimetry models for the ICRP reference pediatric age series. A dissertation presented to the graduate schools of the University of Florida in partial fulfillment of the requirements for the degree of doctor of the philosophy. University of Florida. 2009.
12. Hough M, Johnson P, Rajon D, Jokisch D, Lee C, Bolch W. An image-based skeletal dosimetry model for the ICRP reference adult male–internal electron sources. Phys Med Biol. 2011; 56 (8): 2309–46. DOI: 10.1088/0031-9155/56/8/001. Epub 2011 Mar 22.
13. Bolch WE, Eckerman K, Endo A, et al. ICRP Publication 143: Paediatric Reference Computational Phantoms. Ann ICRP. 2020; 49 (1): 5–297. DOI: 10.1177/0146645320915031.
14. Degteva MO, Tolstykh EI, Shishkina EA, Sharagin PA, Zalyapin VI, Volchkova AY, et al. Stochastic parametric skeletal dosimetry model for humans: General approach and application to active marrow exposure from bone-seeking beta-particle emitters. PLoS ONE. 2021; 16 (10): e0257605. Available from: https://doi.org/10.1371/journal.pone.0257605.
15. Djogteva MO, Shishkina EA, Tolstyh EI, Zaljapin VI, Sharagin PA, Smit MA,

i dr. Metodologicheskij podhod k razrabotke dozimetricheskih modelej skeleta cheloveka dlja beta-izluchajushhih radionuklidov. Radiacionnaja gigiena. 2019; 12 (2). DOI: 10.21514/1998-426X-2019-12-2-66-75. Russian.
16. Volchkova AYu, Sharagin PA, Shishkina EA. Internal bone marrow dosimetry: the effect of the exposure due to 90Sr incorporated in the adjacent bone segments. Bulletin of the South Ural State University. Ser. Mathematical Modelling, Programming & Computer Software. 2022; 15 (4): 44–58. DOI: 10.14529/mmp220404.
17. Shishkina EA, Sharagin PA, Volchkova AYu. Analiticheskoe opisanie dozoobrazovanija v kostnom mozge ot 90Sr, inkorporirovannogo v kal'cificirovannyh tkanjah. Voprosy radiacionnoj bezopasnosti. 2021; 3: 72–82. Russian.
18. Silkin SS, Krestinina LYu, Starcev NV, Akleev AV. Ural'skaja kogorta avarijno-obluchennogo naselenija. Medicina jekstremal'nyh situacij. 2019; 21 (3): 393–402. Russian.
19. Sharagin PA, Shishkina EA, Tolstykh EI. Computational phantom for red bone marrow dosimetry from incorporated beta emitters in a newborn baby. Extreme Medicine. 2022; 4: 74–82. DOI: 10.47183/mes.2022.045. Russian.
20. Sharagin PA, Shishkina EA, Tolstykh EI. Computational red bone marrow dosimetry phantom of a one-year-old child enabling assessment of exposure due to incorporated beta emitters. Extreme Medicine. 2023; 3: 44–55. DOI: 10.47183/mes.2023.030. Russian.
21. Sharagin PA, Tolstykh EI, Shishkina EA. Computational phantom for a 5-year-old child red bone marrow dosimetry due to incorporated beta emitters. Extreme Medicine. 2023; (4): 79–90. DOI: 10.47183/mes.2023.061. Russian.
22. Cristy M. Active bone marrow distribution as a function of age in humans. Phys Med Biol. 1981; 26 (3): 389–400. 1981.
23. Tolstyh EI, Sharagin PA, Shishkina EA, Volchkova AYu, Degteva MO. Anatomo-morfologicheskij bazis dlja dozimetricheskogo modelirovanija trabekuljarnoj kosti cheloveka s ispol'zovaniem stohasticheskogo parametricheskogo podhoda. Klinicheskij vestnik GNC FMBC im. A. I. Burnazjana. 2022; 3: 25–40. Russian.
24. Tolstyh EI, Sharagin PA, Shishkina EA, Degteva MO. Formirovanie doz obluchenija krasnogo kostnogo mozga cheloveka ot 89,90Sr, ocenka parametrov trabekuljarnoj kosti dlja dozimetricheskogo modelirovanija. V sbornike: Materialy mezhdunarodnoj nauchnoj konferencii «Sovremennye problemy radiobiologii». Belarus', Gomel', 23–24 sentjabrja 2021. 2021; s. 176–179. Russian.
25. Sharagin PA, Tolstyh EI, Shishkina EA, Degteva MO. Dozimetricheskoe modelirovanie kosti dlja osteotropnyh beta-izluchajushhih radionuklidov: razmernye parametry i segmentacija. V sbornike: Materialy mezhdunarodnoj nauchnoj konferencii «Sovremennye problemy radiobiologii». Belarus', Gomel', 23–24 sentjabrja 2021. 2021; s. 200–204. Russian.
26. Sharagin PA, Shishkina EA, Tolstykh EI, Volchkova AYu, Smith MA, Degteva MO. Segmentation of hematopoietic sites of human skeleton for calculations of dose to active marrow exposed to bone-seeking radionuclides. In: RAD Conference Proceedings. 2018; (3): 154–58. DOI: 10.21175/RadProc.2018.33.
27. Valentin J. Basic anatomical and physiological data for use in radiological protection: reference values. Annals of the ICRP. Annals of the ICRP. 2002; 32 (3–4): 1–277.
28. Woodard HQ and White DR. The composition of body tissues. Br J Ru&ol. 1986; 59: 1209–18.
29. Shishkina EA, Timofeev YS, Volchkova AY, Sharagin PA, Zalyapin VI, Degteva MO, et al. Trabecula: A Random Generator of Computational Phantoms for Bone Marrow Dosimetry. Health Phys. 2020; 118 (1): 53–59. DOI: 10.1097/HP.0000000000001127.
30. Zalyapin VI, Timofeev YuS, Shishkina EA. A parametric stochastic model of bone geometry. Bulletin of Southern Urals State University, Issue «Mathematical Modelling. Programming & Computer Software» (SUSU MMCS) 2018; 11 (2): 44–57. DOI: 10.14529/mmp180204.
31. Robinson RA. Chemical analysis and electron microscopy of bone. In: Bone as a tissue, ed. by Rodahl K, Nicholson JT, Brown EM. New York: McGraw-Hill, 1960; p. 186–250.
32. Vogler JB 3rd, Murphy WA. Bone marrow imaging. Radiology. 1988; 168 (3): 679–93.
33. Vande Berg BC, Malghem J, Lecouvet FE, Maldague B. Magnetic resonance imaging of the normal bone marrow. Skeletal Radiology. 1998; 27: 471–83.
34. Vande Berg BC, Malghem J, Lecouvet FE, Maldague B. Magnetic resonance imaging of normal bone marrow. Eur Radiol. 1998; 8 (8): 1327–34.
35. Taccone A, Oddone M, Dell'Acqua AD, Occhi M, Ciccone MA. MRI "road-map" of normal age-related bone marrow. II. Thorax, pelvis and extremities. Pediatr Radiol. 1995; 25 (8): 596–606. PubMed PMID: 8570312.
36. Taccone A, Oddone M, Occhi M, Dell'Acqua AD, Ciccone MA. MRI "road-map" of normal age-related bone marrow. I. Cranial bone and spine. Pediatr Radiol. 1995; 25 (8): 588–95. PubMed PMID: 8570311.
37. Milovanovic P, Djonic D, Hahn M, Amling M, Busse B, Djuric M. Region-dependent patterns of trabecular bone growth in the human proximal femur: A study of 3D bone microarchitecture from early postnatal to late childhood period. Am J Phys Anthropol. 2017; 164 (2): 281–91. DOI: 10.1002/ajpa.23268. Epub 2017 Jun 20.
38. Ryan TM, Krovitz GE. Trabecular bone ontogeny in the human proximal femur. J Hum Evol. 2006; 51 (6): 591–602.
39. Cunningham C, Scheuer L, Black S. Developmental Juvenile Osteology. Second Edition. Elsevier Academic Press. 2016.
40. man JH, Ketcham RA. Patterns in ontogeny of human trabecular bone from SunWatch Village in the Prehistoric Ohio Valley: general features of microarchitectural change. Am J Phys Anthropol. 2009; 138 (3): 318–32. DOI: 10.1002/ajpa.20931. PubMed PMID: 18785633.
41. Glorieux FH, Travers R, Taylor A, Bowen JR, Rauch F, Norman M, Parfitt AM. Normative data for iliac bone histomorphometry in growing children. Bone. 2000; 26 (2): 103–9.
42. Gao S, Ren L, Qui R, Wu Z, Li C, Li J. Electron absorbed fractions in an image-based microscopic skeletal dosimetry model of chinese adult male. Radiat Prot Dosimetry. 2017; 175 (4): 450–59.
43. Pafundi D. Image-based skeletal tissues and electron dosimetry models for the ICRP reference pediatric age series. A dissertation presented to the graduate schools of the University of Florida in partial fulfillment of the requirements for the degree of doctor of the philosophy University of Florida. 2009.
44. Ryan TM, Raichlen DA, Gosman JH. Structural and Mechanical Changes in Trabecular Bone during Early Development in the Human Femur and Humerus. Chapter 12. In: Building Bones: Bone Formation and Development in Anthropology. Cambridge University Press 2017; 281–302. Available from: https://doi.org/10.1017/9781316388907.013.
45. Milenković P. Age Estimation Based on Analyses of Sternal End of Clavicle and the First Costal Cartilage Doctoral Dissertation. University OF Belgrade School of Medicine. Belgrade, 2013.
46. Kirmani S, Christen D, van Lenthe GH, Fischer PR, Bouxsein ML, McCready LK, Melton LJ 3rd, Riggs BL, Amin S, Müller R, Khosla S. Bone structure at the distal radius during adolescent growth. J Bone Miner Res. 2009; 24 (6): 1033–42. DOI: 10.1359/jbmr.081255.
47. Mitchell DM, Caksa S, Yuan A, Bouxsein ML, Misra M, Burnett-Bowie SM. Trabecular Bone Morphology Correlates Wwith Skeletal Maturity and Body Composition in Healthy Adolescent Girls. J Clin Endocrinol Metab. 2018; 103 (1): 336–45. DOI: 10.1210/jc.2017-01785.
48. Li X, Williams P, Curry EJ, Choi D, Craig EV, Warren RF, et al. Trabecular Bone Microarchitecture and Characteristics in Different Regions of the Glenoid. Orthopedics. 2015; 38 (3): 163–68.
49. Knowles NK, G Langohr GD, Faieghi M, Nelson A, Ferreira LM. Development of a validated glenoid trabecular density-modulus relationship. J Mech Behav Biomed Mater. 2019; 90: 140–45. DOI: 10.1016/j.jmbbm.2018.10.013.
50. Jun BJ, Vasanji A, Ricchetti ET, Rodriguez E, Subhas N, Li ZM, Iannotti JP.Quantification of regional variations in glenoid trabecular bone architecture and mineralization using clinical computed tomography images. J Orthop Res. 2018; 36 (1): 85–96. DOI: 10.1002/jor.23620.
51. Frich LH, Odgaard A, Dalstra M. Glenoid bone architecture J Shoulder Elbow Surg. 1998; 7 (4): 356–61.
52. Kneissel M, Roschger P, Steiner W, et al. Cancellous bone structure in the growing and aging lumbar spine in a historic Nubian population. Calcif Tissue Int. 1997; 61 (2): 95–100. DOI:

10.1007/s002239900302.
53. Arbabi A. A quantitative analysis of the structure of human sternum. J Med Phys. 2009; 34 (2): 80–86.
54. Bartl R, Frisch B. Biopsy of bone in internal medicine — an atlas and sourcebook. Kluwer Academic Publishers, Dordrecht. London, 1993.
55. Baur-Melnyk A. Magnetic Resonance Imaging of the Bone Marrow. Springer Science & Business Media, 2012.
56. Byers S, Moore AJ, Byard RW, Fazzalari NL. Quantitative histomorphometric analysis of the human growth plate from birth to adolescence. Bone. 2000; 27 (4): 495–501.
57. Florence JL. Linear and cortical bone dimensions as indicators of health status in subadults from the Milwaukee County Poor Farm Cemetery. M.A., University of Colorado at Denver, 2007.
58. Maresh MM. Measurements from roentgenograms. In: R.W. McCammon, editor. Human Growth and Development. Springfield, IL: Charles C. Thomas, 1970; 157–200.
59. Singh SP, Malhotra P, Sidhu LS, Singh PP. Skeletal Frame Size of Spitian Children. Journal of Human Ecology. 2007; 21 (3): 227–30.
60. Zivicnjak M, Smolej Narancić N, Szirovicza L, Franke D, Hrenović J, Bisof V, Tomas Z, Skarić-Jurić T. Gender-specific growth patterns of transversal body dimensions in Croatian children and youth (2 to 18 years of age). Coll Antropol. 2008; 32 (2): 419–31. PubMed PMID: 18756891.
61. Svadovskij BS. Vozrastnaja perestrojka kostnoj tkani. O roste i razvitii diafizov plechevoj i bedrennoj kostej. M.: Izd-vo akad. ped. nauk RSFSR, 1961; 110 s.
62. Miles AEW. Growth Curves of Immature Bones from a Scottish Island Population of Sixteenth to mid-Nineteenth Century: Limb-bone Diaphyses and Some Bones of the Hand and Foot. International Journal of Osteoarcheology. 1994; 4: 121–36.
63. Gosman JH, Ketcham RA. Patterns in ontogeny of human trabecular bone from SunWatch Village in the Prehistoric Ohio Valley: general features of microarchitectural change. Am J Phys Anthropol. 2009; 138 (3): 318–32. DOI:10.1002/ajpa.20931. PubMed PMID: 18785633.
64. Petit MA, McKay HA, MacKelvie KJ, Heinonen A, Khan KM, Beck TJ. A randomized school-based jumping intervention confers site and maturity-specific benefits on bone structural properties in girls: a hip structural analysis study. J Bone Miner Res. 2002; 17 (3): 363–72. PubMed PMID: 11874228.
65. Danforth ME, Wrobel GD, Armstrong CW, Swanson D. Juvenile age estimation using diaphyseal long bone lengths among ancient Maya populations. Latin American Antiquity. 2017; 20 (1): 3–13.
66. Beresheim AC, Pfeiffer S, Grynpas M. Ontogenetic changes to bone microstructure in an archaeologically derived sample of human ribs. J Anat. 2019. DOI: 10.1111/joa.13116.
67. Pfeiffer S. Cortical Bone Histology in Juveniles. Available from: https://www.researchgate.net/publication/303179375_Cortical_bone_histology_in_Juveniles
68. Hresko AM, Hinchcliff EM, Deckey DG, Hresko MT. Developmental sacral morphology: MR study from infancy to skeletal maturity. Eur Spine J. 2020; Available from: https://doi.org/10.1007/s00586-020-06350-6.
69. Kuznecov LE. Perelomy taza u detej (morfologija, biomehanika, diagnostika). Moskva: Folium, 1994; 192 s. Russian.
70. Bernert Zs, Évinger S, Hajdu T. New data on the biological age estimation of children using bone measurements based on historical populations from the Carpathian Basin. Annales Historico-Naturales Musei Nationalis Hungarici. 2007; 99: 199–206.
71. Sadofyeva VI. Normal X-ray anatomy of the bone-joint system of children. Leningrad “Medicine” Leningrad branch 1990. Russian
72. White TD, Black MT, Folkens PA. Human osteology: Third edition. Human Osteology: Third Edition. 2011; 1–662.
73. Mavrych V, Bolgova O, Ganguly P and Kashchenko S. Age-Related Changes of Lumbar Vertebral Body Morphometry. Austin J Anat. 2014; 1 (3): 7.
74. Kindler JM, Pollock NK, Laing EM, et al. Insulin Resistance and the IGF-I-Cortical Bone Relationship in Children Ages 9 to 13 Years. J Bone Miner Res. 2017; 32 (7): 1537–1545. DOI: 10.1002/jbmr.3132.
75. Farr JN, Khosla S. Skeletal changes through the lifespan–from growth to senescence. Nat Rev Endocrinol. 2015; 11 (9): 513–21. DOI: 10.1038/nrendo. 2015.89. Epub 2015 Jun 2. Review. PubMed PMID: 26032105; PubMed Central PMCID: PMC4822419.
76. Gindhart PS. Growth Standards for the Tibia and Radius in Children Aged One Month through Eighteen Years. Am J Phys Anthrop. 1973; 39: 41–48.
77. Lopez-Costas O, Rissech C, Trancho G, Turbón D. Postnatal ontogenesis of the tibia. Implications for age and sex estimation. Forensic Sci Int. 2012; 214 (1–3): 207.e1–11. DOI: 10.1016/j.forsciint.2011.07.038. Epub 2011. PubMed PMID: 21862250.
78. Blake KAS. An investigation of sex determination from the subadult pelvis: A morphometric analysis. Doctoral Dissertation, University of Pittsburgh, 2011.
79. Cunningham CA, Black SM. Iliac cortical thickness in the neonate — the gradient effect. J Anat. 2009a Sep; 215 (3): 364–70. DOI: 10.1111/j.1469-7580.2009.01112.x.
80. Cunningham CA, Black SM. Anticipating bipedalism: trabecular organization in the newborn ilium. J Anat. 2009b Jun; 214 (6): 817–29. DOI: 10.1111/j.1469-7580.2009.01073.x
81. Rissech C, Garcıa M, Malgosa A. Sex and age diagnosis by ischium morphometric analysis. Forensic Science International. 2003; 135: 188–96.
82. Rissech C, Malgosa A. Pubis growth study: Applicability in sexual and age diagnostic. Forensic Science International. 2007; 173: 137–45.
83. Corron L, Marchal F, Condemi S, Chaumoître K, Adalian P. A New Approach of Juvenile Age Estimation using Measurements of the Ilium and Multivariate Adaptive Regression Splines (MARS) Models for Better Age Prediction. Forensic Sci. 2017; 62 (1): 18–29. DOI: 10.1111/1556-4029.13224.
84. Parfitt AM, Travers R, Rauch F, Glorieux FH. Structural and cellular changes during bone growth in healthy children. Bone. 2000; 27 (4): 487–94. PMID: 11033443.
85. Schnitzler CM, Mesquita JM, Pettifor JM. Cortical bone development in black and white South African children: iliac crest histomorphometry. Bone. 2009; 44 (4): 603–11. DOI: 10.1016/j.bone.2008.12.009.
86. De Boer HH, Van der Merwe AE, Soerdjbalie-Maikoe VV. Human cranial vault thickness in a contemporary sample of 1097 autopsy cases: relation to body weight, stature, age, sex and ancestry. Int J Legal Med. 2016; 130 (5): 1371–7. DOI: 10.1007/s00414-016-1324-5.
87. Margulies S, Coats B. Experimental Injury Biomechanics of the Pediatric Head and Brain. Chapter 4 in: Pediatric Injury Biomechanics Springer Science + Business Media New York. 2013; 157–90.
88. McGraw MA, Mehlman CT, Lindsell CJ, Kirby CL. Postnatal growth of the clavicle: birth to eighteen years of age. Journal of Pediatric Orthopedics. 2009; 29: 937
89. Bernat A, Huysmans T, Van Glabbeek F, Sijbers J, Gielen J, Van Tongel A. The anatomy of the clavicle: a three-dimensional cadaveric study. Clin Anat. 2014; 27 (5): 712–23
90. Corron L. Juvenile age estimation in physical anthropology: A critical review of existing methods and the application of two standardised methodological approaches. Biological anthropology. Aix-Marseille Universite. English, 2016.
91. Saunders S, Hoppa R, Southern R. Diaphyseal growth in a nineteenth-century skeletal sample of subadults from St Thomas’ Church, Belleville, Ontario. International Journal of Osteoarchaeology. 1993; 3: 265–81.
92. Badr El Dine F, Hassan H. Ontogenetic study of the scapula among some Egyptians: Forensic implications in age and sex estimation using Multidetector Computed Tomography, Egyptian Journal of Forensic Sciences. 2015; 6 (2): 56–77.
93. Rissech C, Black S. Scapular development from neonatal period to skeletal maturity. A preliminary study. Int J Osteoarchaeol. 2007; 17: 451–64.
94. Bayaroğulları H, Yengil E, Davran R, Ağlagül E, Karazincir S, Balcı A. Evaluation of the postnatal development of the sternum and sternal variations using multidetector CT. Diagn Interv Radiol. 2014; 20 (1): 82–9.
95. Weaver AA, Schoell SL, Nguyen CM, Lynch SK, Stitzel JD. Morphometric analysis of variation in the sternum with sex and age. J Morphol. 2014; 275 (11): 1284–99.
96. Johnson KT, Al-Holou WN, Anderson RC, Wilson TJ, Karnati T, et al. Morphometric analysis of the developing pediatric cervical spine. J Neurosurg Pediatr. 2016; 18 (3): 377–89. DOI: 10.3171/2016.3.PEDS1612. Epub 2016 May 27. PubMed PMID: 27231821.

97. Caldas Md P, Ambrosano GM, Haiter Neto F. New formula to objectively evaluate skeletal maturation using lateral cephalometric radiographs. Braz Oral Res. 2007; 21 (4): 330–5. PubMed PMID: 18060260
98. Peters JR, Chandrasekaran C, Robinson LF, Servaes SE, Campbell RM Jr, Balasubramanian S. Age- and gender-related changes in pediatric thoracic vertebral morphology. Spine J. 2015; 15 (5): 1000–1020. DOI: 10.1016/j.spinee.2015.01.016.
99. Peters JR, Servaes SE, Cahill PJ, Balasubramanian S. Morphology and growth of the pediatric lumbar vertebrae. Spine J. 2021; 21 (4): 682–97. DOI: 10.1016/j.spinee.2020.10.029.
100. Newman SL, Gowland RL. The use of non-adult vertebral dimensions as indicators of growth disruption and non-specific health stress in skeletal populations. American journal of physical anthropology. 2015; 158 (1): 155–64.
101. Comeau A. Age-related Changes in Geometric Characteristics of the Pediatric Thoracic Cage and Comparison of Thorax Shape with a Pediatric CPR Manikin. PhD thesis. 2010
102. Knirsch W, Kurtz C, Häffner N, Langer M, Kececioglu D. Normal values of the sagittal diameter of the lumbar spine (vertebral body and dural sac) in children measured by MRI. Pediatr Radiol. 2005; 35: 419–24. Available from: https://doi.org/10.1007/s00247-004-1382-6.

Литература

1. Sources and effects of ionizing radiation. UNSCEAR 2000 Report to the General Assembly, with Scientific Annexes/ United Nations. New York, 2000; 1229 c.
2. Degteva MO, Shagina NB, Vorobiova MI, Shishkina EA, Tolstykh EI, Akleyev AV. Contemporary Understanding of Radioactive Contamination of the Techa River in 1949–1956. Radiats Biol Radioecol. 2016; 56 (5): 523–34. PMID: 30703313.
3. Krestinina LY, Epifanova S, Silkin S, Mikryukova L, Degteva M, Shagina N, et al. Chronic low-dose exposure in the Techa River Cohort: risk of mortality from circulatory diseases. Radiat Environ Biophys. 2013; 52 (1): 47–57. DOI: 10.1007/s00411-012-0438-5. Epub 2012 Nov 4.
4. Аклеев А. В. Хронический лучевой синдром у жителей прибрежных сел реки Теча. Челябинск: Книга, 2012; 464 с.
5. Preston DL, Sokolnikov ME, Krestinina LY, Stram DO. Estimates of Radiation Effects on Cancer Risks in the Mayak Worker, Techa River and Atomic Bomb Survivor Studies. Radiat Prot Dosimetry. 2017; 173 (1–3): 26–31. DOI: 10.1093/rpd/ncw316.
6. Degteva MO, Napier BA, Tolstykh EI, et al. Enhancements in the Techa River Dosimetry System: TRDS-2016D Code for Reconstruction of Deterministic Estimates of Dose From Environmental Exposures. Health Phys. 2019; 117 (4): 378–87. DOI: 10.1097/HP.0000000000001067.
7. Spiers FW, Beddoe AH, Whitwell JR. Mean skeletal dose factors for beta-particle emitters in human bone. Part I: volume-seeking radionuclides. The British journal of radiology. 1978; 51 (608): 622–7.
8. O'Reilly SE, DeWeese LS, Maynard MR, Rajon DA, Wayson MB, Marshall EL, et al. An 13 image-based skeletal dosimetry model for the ICRP reference adult female-internal electron 14 sources. Phys Med Biol. 2016; 61 (24): 8794–24. Epub 2016 Nov 29.
9. Xu XG, Chao TC, Bozkurt A. VIP-Man: an image-based whole-body adult male model constructed from color photographs of the Visible Human Project for multi-particle Monte Carlo calculations. Health Phys. 2000; 78 (5): 476–86. DOI: 10.1097/00004032-200005000-00003. PMID: 10772019.
10. Shah AP, Bolch WE, Rajon DA, Patton PW, Jokisch DW. A paired-image radiation transport model for skeletal dosimetry. J Nucl Med. 2005; 46 (2): 344–53. PMID: 15695796.
11. Pafundi D. Image-based skeletal tissues and electron dosimetry models for the ICRP reference pediatric age series. A dissertation presented to the graduate schools of the University of Florida in partial fulfillment of the requirements for the degree of doctor of the philosophy. University of Florida. 2009.
12. Hough M, Johnson P, Rajon D, Jokisch D, Lee C, Bolch W. An image-based skeletal dosimetry model for the ICRP reference adult male–internal electron sources. Phys Med Biol. 2011; 56 (8): 2309–46. DOI: 10.1088/0031-9155/56/8/001. Epub 2011 Mar 22.
13. Bolch WE, Eckerman K, Endo A, et al. ICRP Publication 143: Paediatric Reference Computational Phantoms. Ann ICRP. 2020; 49 (1): 5–297. DOI: 10.1177/0146645320915031.
14. Degteva MO, Tolstykh EI, Shishkina EA, Sharagin PA, Zalyapin VI, Volchkova AY, et al. Stochastic parametric skeletal dosimetry model for humans: General approach and application to active marrow exposure from bone-seeking beta-particle emitters. PLoS ONE. 2021; 16 (10): e0257605. Available from: https://doi.org/10.1371/journal.pone.0257605.
15. Дёгтева М. О., Шишкина Е. А., Толстых Е. И., Заляпин В. И., Шарагин П. А., Смит М. А., и др. Методологический подход к разработке дозиметрических моделей скелета человека для бета-излучающих радионуклидов. Радиационная гигиена. 2019; 12 (2). DOI: 10.21514/1998-426X-2019-12-2-66-75.
16. Volchkova AYu, Sharagin PA, Shishkina EA. Internal bone marrow dosimetry: the effect of the exposure due to 90Sr incorporated in the adjacent bone segments. Bulletin of the South Ural State University. Ser. Mathematical Modelling, Programming & Computer Software. 2022; 15 (4): 44–58. DOI: 10.14529/mmp220404.
17. Шишкина Е. А., Шарагин П. А., Волчкова А. Ю. Аналитическое описание дозообразования в костном мозге от 90Sr, инкорпорированного в кальцифицированных тканях. Вопросы радиационной безопасности. 2021; 3: 72–82.
18. Силкин С. С., Крестинина Л. Ю., Старцев Н. В, Аклеев А. В. Уральская когорта аварийно-облученного населения. Медицина экстремальных ситуаций. 2019; 21 (3): 393–402.
19. Шарагин П. А., Шишкина Е. А., Толстых Е. И. Вычислительный фантом для дозиметрии красного костного мозга новорожденного ребенка от инкорпорированных бета-излучателей. Медицина экстремальных ситуаций. 2022; (4): 74–82. DOI: 10.47183/mes.2022.045.
20. Шарагин, П. А., Шишкина, Е. А., Толстых, Е. И. Вычислительный фантом для дозиметрии красного костного мозга годовалого ребенка от инкорпорированных бета-излучателей. Медицина экстремальных ситуаций. 2023, (3): 44 –55. DOI: 10.47183/mes.2023.030.
21. Шарагин П. А., Толстых Е. И., Шишкина Е. А. Вычислительный фантом для дозиметрии красного костного мозга пятилетнего ребенка от инкорпорированных бета-излучателей. Медицина экстремальных ситуаций. 2023; (4): 86–97. DOI: 10.47183/mes.2023.061.
22. Cristy M. Active bone marrow distribution as a function of age in humans. Phys Med Biol. 1981; 26 (3): 389–400. 1981.
23. Толстых Е. И., Шарагин П. А., Шишкина Е. А., Волчкова А. Ю. Дегтева М. О. Анатомо-морфологический базис для дозиметрического моделирования трабекулярной кости человека с использованием стохастического параметрического подхода. Клинический вестник ГНЦ ФМБЦ им. А. И. Бурназяна. 2022; 3: 25–40.
24. Толстых Е. И., Шарагин П. А., Шишкина Е. А., Дегтева М. О. Формирование доз облучения красного костного мозга человека от ^{89,90}Sr, оценка параметров трабекулярной кости для дозиметрического моделирования. В сборнике: Материалы международной научной конференции «Современные проблемы радиобиологии». Беларусь, Гомель, 23–24 сентября 2021. 2021; с. 176–179.
25. Шарагин П. А., Толстых Е. И., Шишкина Е. А., Дегтева М. О. Дозиметрическое моделирование кости для остеотропных бета-излучающих радионуклидов: размерные параметры и сегментация. В сборнике: Материалы международной научной конференции «Современные проблемы радиобиологии». Беларусь, Гомель, 23–24 сентября 2021. 2021; с. 200–204.
26. Sharagin PA, Shishkina EA, Tolstykh EI, Volchkova AYu, Smith MA, Degteva MO. Segmentation of hematopoietic sites of human skeleton for calculations of dose to active marrow exposed to bone-seeking radionuclides. In: RAD Conference Proceedings. 2018; (3): 154–58. DOI: 10.21175/RadProc.2018.33.
27. Valentin J. Basic anatomical and physiological data for use in

radiological protection: reference values. Annals of the ICRP. Annals of the ICRP. 2002; 32 (3–4): 1–277.
28. Woodard HQ and White DR. The composition of body tissues. Br J Ru&ol. 1986; 59: 1209–18.
29. Shishkina EA, Timofeev YS, Volchkova AY, Sharagin PA, Zalyapin VI, Degteva MO, et al. Trabecula: A Random Generator of Computational Phantoms for Bone Marrow Dosimetry. Health Phys. 2020; 118 (1): 53–59. DOI: 10.1097/HP.0000000000001127.
30. Zalyapin VI, Timofeev YuS, Shishkina EA. A parametric stochastic model of bone geometry. Bulletin of Southern Urals State University, Issue «Mathematical Modelling. Programming & Computer Software» (SUSU MMCS) 2018; 11 (2): 44–57. DOI: 10.14529/mmp180204.
31. Robinson RA. Chemical analysis and electron microscopy of bone. In: Bone as a tissue, ed. by Rodahl K, Nicholson JT, Brown EM. New York: McGraw-Hill, 1960; p. 186–250.
32. Vogler JB 3rd, Murphy WA. Bone marrow imaging. Radiology. 1988; 168 (3): 679–93.
33. Vande Berg BC, Malghem J, Lecouvet FE, Maldague B. Magnetic resonance imaging of the normal bone marrow. Skeletal Radiology. 1998; 27: 471–83.
34. Vande Berg BC, Malghem J, Lecouvet FE, Maldague B. Magnetic resonance imaging of normal bone marrow. Eur Radiol. 1998; 8 (8): 1327–34.
35. Taccone A, Oddone M, Dell'Acqua AD, Occhi M, Ciccone MA. MRI "road-map" of normal age-related bone marrow. II. Thorax, pelvis and extremities. Pediatr Radiol. 1995; 25 (8): 596–606. PubMed PMID: 8570312.
36. Taccone A, Oddone M, Occhi M, Dell'Acqua AD, Ciccone MA. MRI "road-map" of normal age-related bone marrow. I. Cranial bone and spine. Pediatr Radiol. 1995; 25 (8): 588–95. PubMed PMID: 8570311.
37. Milovanovic P, Djonic D, Hahn M, Amling M, Busse B, Djuric M. Region-dependent patterns of trabecular bone growth in the human proximal femur: A study of 3D bone microarchitecture from early postnatal to late childhood period. Am J Phys Anthropol. 2017; 164 (2): 281–91. DOI: 10.1002/ajpa.23268. Epub 2017 Jun 20.
38. Ryan TM, Krovitz GE. Trabecular bone ontogeny in the human proximal femur. J Hum Evol. 2006; 51 (6): 591–602.
39. Cunningham C, Scheuer L, Black S. Developmental Juvenile Osteology. Second Edition. Elsevier Academic Press. 2016.
40. man JH, Ketcham RA. Patterns in ontogeny of human trabecular bone from SunWatch Village in the Prehistoric Ohio Valley: general features of microarchitectural change. Am J Phys Anthropol. 2009; 138 (3): 318–32. DOI: 10.1002/ajpa.20931. PubMed PMID: 18785633.
41. Glorieux FH, Travers R, Taylor A, Bowen JR, Rauch F, Norman M, Parfitt AM. Normative data for iliac bone histomorphometry in growing children. Bone. 2000; 26 (2): 103–9.
42. Gao S, Ren L, Qui R, Wu Z, Li C, Li J. Electron absorbed fractions in an image-based microscopic skeletal dosimetry model of chinese adult male. Radiat Prot Dosimetry. 2017; 175 (4): 450–59.
43. Pafundi D. Image-based skeletal tissues and electron dosimetry models for the ICRP reference pediatric age series. A dissertation presented to the graduate schools of the University of Florida in partial fulfillment of the requirements for the degree of doctor of the philosophy University of Florida. 2009.
44. Ryan TM, Raichlen DA, Gosman JH. Structural and Mechanical Changes in Trabecular Bone during Early Development in the Human Femur and Humerus. Chapter 12. In: Building Bones: Bone Formation and Development in Anthropology. Cambridge University Press 2017; 281–302. Available from: https://doi.org/10.1017/9781316388907.013.
45. Milenković P. Age Estimation Based on Analyses of Sternal End of Clavicle and the First Costal Cartilage Doctoral Dissertation. University OF Belgrade School of Medicine. Belgrade, 2013.
46. Kirmani S, Christen D, van Lenthe GH, Fischer PR, Bouxsein ML, McCready LK, Melton LJ 3rd, Riggs BL, Amin S, Müller R, Khosla S. Bone structure at the distal radius during adolescent growth. J Bone Miner Res. 2009; 24 (6): 1033–42. DOI: 10.1359/jbmr.081255.
47. Mitchell DM, Caksa S, Yuan A, Bouxsein ML, Misra M, Burnett-Bowie SM. Trabecular Bone Morphology Correlates Wwith Skeletal Maturity and Body Composition in Healthy Adolescent Girls. J Clin Endocrinol Metab. 2018; 103 (1): 336–45. DOI: 10.1210/jc.2017-01785.
48. Li X, Williams P, Curry EJ, Choi D, Craig EV, Warren RF, et al. Trabecular Bone Microarchitecture and Characteristics in Different Regions of the Glenoid. Orthopedics. 2015; 38 (3): 163–68.
49. Knowles NK, G Langohr GD, Faieghi M, Nelson A, Ferreira LM. Development of a validated glenoid trabecular density-modulus relationship. J Mech Behav Biomed Mater. 2019; 90: 140–45. DOI: 10.1016/j.jmbbm.2018.10.013.
50. Jun BJ, Vasanji A, Ricchetti ET, Rodriguez E, Subhas N, Li ZM, Iannotti JP.Quantification of regional variations in glenoid trabecular bone architecture and mineralization using clinical computed tomography images. J Orthop Res. 2018; 36 (1): 85–96. DOI: 10.1002/jor.23620.
51. Frich LH, Odgaard A, Dalstra M. Glenoid bone architecture J Shoulder Elbow Surg. 1998; 7 (4): 356–61.
52. Kneissel M, Roschger P, Steiner W, et al. Cancellous bone structure in the growing and aging lumbar spine in a historic Nubian population. Calcif Tissue Int. 1997; 61 (2): 95–100. DOI: 10.1007/s002239900302.
53. Arbabi A. A quantitative analysis of the structure of human sternum. J Med Phys. 2009; 34 (2): 80–86.
54. Bartl R, Frisch B. Biopsy of bone in internal medicine — an atlas and sourcebook. Kluwer Academic Publishers, Dordrecht. London, 1993.
55. Baur-Melnyk A. Magnetic Resonance Imaging of the Bone Marrow. Springer Science & Business Media, 2012.
56. Byers S, Moore AJ, Byard RW, Fazzalari NL. Quantitative histomorphometric analysis of the human growth plate from birth to adolescence. Bone. 2000; 27 (4): 495–501.
57. Florence JL. Linear and cortical bone dimensions as indicators of health status in subadults from the Milwaukee County Poor Farm Cemetery. M.A., University of Colorado at Denver, 2007.
58. Maresh MM. Measurements from roentgenograms. In: R.W. McCammon, editor. Human Growth and Development. Springfield, IL: Charles C. Thomas, 1970; 157–200.
59. Singh SP, Malhotra P, Sidhu LS, Singh PP. Skeletal Frame Size of Spitian Children. Journal of Human Ecology. 2007; 21 (3): 227–30.
60. Zivicnjak M, Smolej Narancić N, Szirovicza L, Franke D, Hrenović J, Bisof V, Tomas Z, Skarić-Jurić T. Gender-specific growth patterns of transversal body dimensions in Croatian children and youth (2 to 18 years of age). Coll Antropol. 2008; 32 (2): 419–31. PubMed PMID: 18756891.
61. Свадовский Б. С. Возрастная перестройка костной ткани. О росте и развитии диафизов плечевой и бедренной костей. М.: Изд-во акад. пед. наук РСФСР, 1961; 110 с.
62. Miles AEW. Growth Curves of Immature Bones from a Scottish Island Population of Sixteenth to mid-Nineteenth Century: Limb-bone Diaphyses and Some Bones of the Hand and Foot. International Journal of Osteoarcheology. 1994; 4: 121–36.
63. Gosman JH, Ketcham RA. Patterns in ontogeny of human trabecular bone from SunWatch Village in the Prehistoric Ohio Valley: general features of microarchitectural change. Am J Phys Anthropol. 2009; 138 (3): 318–32. DOI:10.1002/ajpa.20931. PubMed PMID: 18785633.
64. Petit MA, McKay HA, MacKelvie KJ, Heinonen A, Khan KM, Beck TJ. A randomized school-based jumping intervention confers site and maturity-specific benefits on bone structural properties in girls: a hip structural analysis study. J Bone Miner Res. 2002; 17 (3): 363–72. PubMed PMID: 11874228.
65. Danforth ME, Wrobel GD, Armstrong CW, Swanson D. Juvenile age estimation using diaphyseal long bone lengths among ancient Maya populations. Latin American Antiquity. 2017; 20 (1): 3–13.
66. Beresheim AC, Pfeiffer S, Grynpas M. Ontogenetic changes to bone microstructure in an archaeologically derived sample of human ribs. J Anat. 2019. DOI: 10.1111/joa.13116.
67. Pfeiffer S. Cortical Bone Histology in Juveniles. Available from: https://www.researchgate.net/publication/303179375_Cortical_bone_histology_in_Juveniles
68. Hresko AM, Hinchcliff EM, Deckey DG, Hresko MT. Developmental sacral morphology: MR study from infancy to skeletal maturity. Eur Spine J. 2020; Available from: https://doi.org/10.1007/s00586-020-06350-6.
69. Кузнецов Л. Е. Переломы таза у детей (морфология, биомеханика, диагностика). Москва: Фолиум, 1994; 192 с.
70. Bernert Zs, Évinger S, Hajdu T. New data on the biological

age estimation of children using bone measurements based on historical populations from the Carpathian Basin. Annales Historico-Naturales Musei Nationalis Hungarici. 2007; 99: 199–206.
71. Sadofyeva VI. Normal X-ray anatomy of the bone-joint system of children. Leningrad "Medicine" Leningrad branch 1990. Russian
72. White TD, Black MT, Folkens PA. Human osteology: Third edition. Human Osteology: Third Edition. 2011; 1–662.
73. Mavrych V, Bolgova O, Ganguly P and Kashchenko S. Age-Related Changes of Lumbar Vertebral Body Morphometry. Austin J Anat. 2014; 1 (3): 7.
74. Kindler JM, Pollock NK, Laing EM, et al. Insulin Resistance and the IGF-I-Cortical Bone Relationship in Children Ages 9 to 13 Years. J Bone Miner Res. 2017; 32 (7): 1537–1545. DOI: 10.1002/jbmr.3132.
75. Farr JN, Khosla S. Skeletal changes through the lifespan–from growth to senescence. Nat Rev Endocrinol. 2015; 11 (9): 513–21. DOI: 10.1038/nrendo. 2015.89. Epub 2015 Jun 2. Review. PubMed PMID: 26032105; PubMed Central PMCID: PMC4822419.
76. Gindhart PS. Growth Standards for the Tibia and Radius in Children Aged One Month through Eighteen Years. Am J Phys Anthrop. 1973; 39: 41–48.
77. Lopez-Costas O, Rissech C, Trancho G, Turbón D. Postnatal ontogenesis of the tibia. Implications for age and sex estimation. Forensic Sci Int. 2012; 214 (1–3): 207.e1–11. DOI: 10.1016/j.forsciint.2011.07.038. Epub 2011. PubMed PMID: 21862250.
78. Blake KAS. An investigation of sex determination from the subadult pelvis: A morphometric analysis. Doctoral Dissertation, University of Pittsburgh, 2011.
79. Cunningham CA, Black SM. Iliac cortical thickness in the neonate — the gradient effect. J Anat. 2009a Sep; 215 (3): 364–70. DOI: 10.1111/j.1469-7580.2009.01112.x.
80. Cunningham CA, Black SM. Anticipating bipedalism: trabecular organization in the newborn ilium. J Anat. 2009b Jun; 214 (6): 817–29. DOI: 10.1111/j.1469-7580.2009.01073.x
81. Rissech C, Garcıa M, Malgosa A. Sex and age diagnosis by ischium morphometric analysis. Forensic Science International. 2003; 135: 188–96.
82. Rissech C, Malgosa A. Pubis growth study: Applicability in sexual and age diagnostic. Forensic Science International. 2007; 173: 137–45.
83. Corron L, Marchal F, Condemi S, Chaumoître K, Adalian P. A New Approach of Juvenile Age Estimation using Measurements of the Ilium and Multivariate Adaptive Regression Splines (MARS) Models for Better Age Prediction. Forensic Sci. 2017; 62 (1): 18–29. DOI: 10.1111/1556-4029.13224.
84. Parfitt AM, Travers R, Rauch F, Glorieux FH. Structural and cellular changes during bone growth in healthy children. Bone. 2000; 27 (4): 487–94. PMID: 11033443.
85. Schnitzler CM, Mesquita JM, Pettifor JM. Cortical bone development in black and white South African children: iliac crest histomorphometry. Bone. 2009; 44 (4): 603–11. DOI: 10.1016/j.bone.2008.12.009.
86. De Boer HH, Van der Merwe AE, Soerdjbalie-Maikoe VV. Human cranial vault thickness in a contemporary sample of 1097 autopsy cases: relation to body weight, stature, age, sex and ancestry. Int J Legal Med. 2016; 130 (5): 1371–7. DOI: 10.1007/s00414-016-1324-5.
87. Margulies S, Coats B. Experimental Injury Biomechanics of the Pediatric Head and Brain. Chapter 4 in: Pediatric Injury Biomechanics Springer Science + Business Media New York. 2013; 157–90.
88. McGraw MA, Mehlman CT, Lindsell CJ, Kirby CL. Postnatal growth of the clavicle: birth to eighteen years of age. Journal of Pediatric Orthopedics. 2009; 29: 937
89. Bernat A, Huysmans T, Van Glabbeek F, Sijbers J, Gielen J, Van Tongel A. The anatomy of the clavicle: a three-dimensional cadaveric study. Clin Anat. 2014; 27 (5): 712–23
90. Corron L. Juvenile age estimation in physical anthropology: A critical review of existing methods and the application of two standardised methodological approaches. Biological anthropology. Aix-Marseille Universite. English, 2016.
91. Saunders S, Hoppa R, Southern R. Diaphyseal growth in a nineteenth-century skeletal sample of subadults from St Thomas' Church, Belleville, Ontario. International Journal of Osteoarchaeology. 1993; 3: 265–81.
92. Badr El Dine F, Hassan H. Ontogenetic study of the scapula among some Egyptians: Forensic implications in age and sex estimation using Multidetector Computed Tomography, Egyptian Journal of Forensic Sciences. 2015; 6 (2): 56–77.
93. Rissech C, Black S. Scapular development from neonatal period to skeletal maturity. A preliminary study. Int J Osteoarchaeol. 2007; 17: 451–64.
94. Bayaroğulları H, Yengil E, Davran R, Ağlagül E, Karazincir S, Balcı A. Evaluation of the postnatal development of the sternum and sternal variations using multidetector CT. Diagn Interv Radiol. 2014; 20 (1): 82–9.
95. Weaver AA, Schoell SL, Nguyen CM, Lynch SK, Stitzel JD. Morphometric analysis of variation in the sternum with sex and age. J Morphol. 2014; 275 (11): 1284–99.
96. Johnson KT, Al-Holou WN, Anderson RC, Wilson TJ, Karnati T, et al. Morphometric analysis of the developing pediatric cervical spine. J Neurosurg Pediatr. 2016; 18 (3): 377–89. DOI: 10.3171/2016.3.PEDS1612. Epub 2016 May 27. PubMed PMID: 27231821.
97. Caldas Md P, Ambrosano GM, Haiter Neto F. New formula to objectively evaluate skeletal maturation using lateral cephalometric radiographs. Braz Oral Res. 2007; 21 (4): 330–5. PubMed PMID: 18060260
98. Peters JR, Chandrasekaran C, Robinson LF, Servaes SE, Campbell RM Jr, Balasubramanian S. Age- and gender-related changes in pediatric thoracic vertebral morphology. Spine J. 2015; 15 (5): 1000–1020. DOI: 10.1016/j.spinee.2015.01.016.
99. Peters JR, Servaes SE, Cahill PJ, Balasubramanian S. Morphology and growth of the pediatric lumbar vertebrae. Spine J. 2021; 21 (4): 682–97. DOI: 10.1016/j.spinee.2020.10.029.
100. Newman SL, Gowland RL. The use of non-adult vertebral dimensions as indicators of growth disruption and non-specific health stress in skeletal populations. American journal of physical anthropology. 2015; 158 (1): 155–64.
101. Comeau A. Age-related Changes in Geometric Characteristics of the Pediatric Thoracic Cage and Comparison of Thorax Shape with a Pediatric CPR Manikin. PhD thesis. 2010
102. Knirsch W, Kurtz C, Häffner N, Langer M, Kececioglu D. Normal values of the sagittal diameter of the lumbar spine (vertebral body and dural sac) in children measured by MRI. Pediatr Radiol. 2005; 35: 419–24. Available from: https://doi.org/10.1007/s00247-004-1382-6.